Counter-Rotating Open Rotor Noise Predictions Using Immersed Boundary Wall-Modeled Large Eddy Simulations

Man Long Wong*, Aditya S. Ghate, Gaetan K. W. Kenway, Jordan B. Angel, Eren Kiris, and Cetin Kiris
Volcano Platforms Inc., 422 Portage Ave, Palo Alto, CA 94306, USA

Wall-modeled large eddy simulations (WMLES) of the counter-rotating open rotor (CROR) configuration using the historical General Electric (GE) F31/A31 blade set are performed at low-speed takeoff (Mach 0.2, 6487 RPM) and high-speed cruise (Mach 0.78, 6942 RPM) conditions with the GPU-accelerated *Volcano ScaLES* computational fluid dynamics (CFD) solver. The compressible Navier–Stokes equations are solved with an algebraic wall model coupled to a robust immersed-boundary formulation on Cartesian meshes, while the rotor motions are handled using a sliding mesh capability and rotating wall boundary conditions. Two approaches are used to predict acoustics at off-body observers for the two configurations. The hybrid computational fluid dynamics/computational aeroacoustics (CFD/CAA) approach is used for the takeoff case, where the near-field flow and acoustic fields are simulated using large eddy simulations, while the acoustics at observer microphones are radiated using an in-situ Ffowcs Williams and Hawkings acoustic solver. On the other hand, direct noise computation is used for the cruise case, where acoustic propagation from near-body flow field to the acoustic-plate-mounted pressure sensors is simulated directly using the CFD solver. Results of both conditions show reasonable agreement with experimental measurements at the observer locations, capturing the dominant tonal peaks and broadband features. The findings demonstrate the capability of GPU-based WMLES to predict CROR aeroacoustics efficiently and with high fidelity. They also highlight its potential as a practical numerical approach for future noise reduction and propulsion system design studies, enabling simulations on grids with approximately one to two billion grid points using affordable single-node servers equipped with workstation GPUs and achieving turnaround times within a single day.

I. Introduction

Counter-rotating open rotors (CRORs), also referred to as contra-rotating open rotors, were first demonstrated as a viable technology in the 1970s as a solution to the oil crisis. Compared to turbofan engines, it is well known that CROR configurations burn less fuel for short-haul flights because their larger effective bypass ratios and lower flow speeds lead to higher propulsive efficiency. CRORs also exhibit better performance than single-rotating open rotors (SRORs) as the aft rotor can recover part of the azimuthal velocity component of the wake downstream of the front rotor into additional axial thrust. Despite the superior performance of CRORs over turbofan engines and SROR, they did not gain wide acceptance for many years due to the higher levels of noise emitted. The noise from CRORs is generated by numerous tonal and broadband sources and their complex interactions, such as the impingement of the tip vortices from the front rotor blades onto the leading edge of the aft rotor blades, the interaction of each blade's turbulent boundary layer with its trailing edge, the impingement of the front rotor wake onto the rear rotor blade edges, etc. In recent years, there has been a rapid growth in the drone delivery and urban air mobility (UAM) markets, where the payloads carried by these aerial vehicles are also increased by orders of magnitude. To meet the more demanding payload requirements while maintaining very compact drone and UAM designs, CRORs have again become an attractive propulsion concept for these low-speed and short-haul flights in recent years. To analyze and reduce the noise generated by any CROR designs, high-fidelity computational fluid dynamics (CFD) and computational aeroacoustics (CAA) methods are essential. The present work investigates the capability and the accuracy of a state-of-the-art CFD software, Volcano ScaLES, in predicting the aeroacoustics radiation from a model scale version of the General Electric (GE) blade data set with large eddy simulations (LES) using workstation GPUs on single node servers. The data set was the result of the collaboration between NASA Glenn Research Center and the industry partner resulted in several new designs for counter-rotating open rotors with studies focused on both performance and aeroacoustics [1–5]. This CROR data set has been used previously for many numerical studies on CROR acoustics [6–11]. However, most of these studies rely on unsteady

*Corresponding author.

Reynolds averaged Navier–Stokes (URANS) or hybrid Reynolds averaged Navier–Stokes/large eddy simulation (hybrid RANS/LES) methods. In this work, the wall-modeled large eddy simulation (WMLES) approach is adopted where the complex geometries are handled by an algebraic model coupled with a robust immersed boundary method on Cartesian grids. The rotating geometries are simulated with the sliding mesh and rotating wall boundary condition capabilities in the software. Two operating conditions, corresponding to takeoff and cruise, are considered to demonstrate the predictive capabilities of the WMLES solver for aeroacoustics. The takeoff case has a lower freestream Mach number, and the acoustic signals at the observer microphones are obtained using a hybrid strategy. The near-field flow and acoustic fields are simulated with WMLES, while the propagation from the near field to the microphone locations is approximated using an in-situ Ffowcs Williams and Hawkings (FWH) solver. The cruise case, by contrast, involves a higher freestream Mach number and involves acoustic propagation in regions with highly nonlinear phenomena, such as shock waves, between the CROR and the microphones. A direct noise computation approach is adopted where acoustic wave propagation from the CROR to the microphones is simulated directly in the WMLES.

The remainder of this paper is organized as follows. Section II describes the CROR configurations, operating conditions, and experimental data used for validation. Section III presents the details of the simulations, including the numerical methods, computational setup, and design of grids and FWH sampling surfaces. Section IV presents the computational results and discussion for both the takeoff and cruise conditions, including comparisons with available experimental measurements for aerodynamic and aeroacoustic quantities. Finally, Section V summarizes the main findings.

II. Description of Problem

The CROR configuration considered in this work uses the so-called "historical baseline" F31/A31 blade set designed by the GE, which was tested experimentally using the Open Rotor Propulsion Rig (ORPR) during a wind tunnel test campaign of NASA Glenn Research Center [3]. During the test, the aerodynamic performance and acoustics of the one-fifth scale model were measured extensively under a range of operating conditions. The ORPR consists of a forward hub and an aft rotor hub, which support the forward and aft rotor blade rows respectively. In addition, a forward rotating seal is attached to the forward hub, and its trailing edge is located close to the leading edge of the aft rotor hub (see Figure 4 of [3]). For the F31/A31 blade set, the front rotor has 12 blades with a diameter of 0.6518 m (25.66 in.), whereas the aft rotor has 10 blades with diameter of 0.6297 m (24.79 in.). The pitch axes of the two rotors are 0.1991 m (7.84 in.) apart. Further details of the F31/A31 blade set can be found in [3]. A takeoff condition and a cruise condition are studied in the present work. The corresponding geometries are shown in Fig. 1. For the takeoff case, the front and aft blade pitch angles are set to 40.1° and 40.8° respectively. The two rotor rows counter-rotate at 6487 revolutions per minute (RPM) in the NASA's 9- by 15-ft Low Speed Wind Tunnel (LSWT) at $M_\infty = 0.2$, where M_∞ denotes the tunnel Mach number. In the LSWT, there are 18 microphones on a sideline array that is 1.524 m (60 in.) away from the centerline of the rig, as shown in Fig. 1(a). As for the cruise case, the front and aft blade pitch angles are set to 64.4° and 61.8° respectively. The rotor rows counter-rotate at 6942 RPM in the NASA's 8- by 6-ft Supersonic Wind Tunnel (SWT) at $M_\infty = 0.78$. In the SWT, an acoustic plate with 17 flush-mounted pressure sensors is installed to measure the unsteady pressure data. The sensor locations are shown in Fig. 1(b). In the experiments, the plate height can be varied such that the sensor distance from the rotor axis ranges from 0.43 m (16.75 in.) to 1.16 m (45.71 in.). In this work, the plate position corresponding to a distance of 1.16 m from the rotor axis is considered.

III. Details of Simulations

A. Numerical Methods and Computational Solver

All simulations in this work are conducted with a GPU-accelerated numerical solver, Volcano ScaLES, with the compressible Navier–Stokes formulation using a nominally fourth-order accurate finite-difference spatial discretization of the convective fluxes with favorable kinetic energy and entropy consistency properties in turbulent regions, and the viscous flux discretization utilizes a mix of fourth and second order discretizations with improved resolution for high Reynolds number turbulent flows. The subgrid-scale stress tensor is modeled with the Smagorinsky model using the dynamic procedure [12, 13]. With the third-order strong stability preserving (SSP) Runge–Kutta (RK) time stepping method [14, 15], the overall numerical formulation is robust and has low dissipation and high isotropy, making it suitable for LES over a vast range of flow regimes with turbulence and acoustic wave radiation. For applications with discontinuities such as shock waves, a shock-capturing method with physics-based discontinuity sensors can be

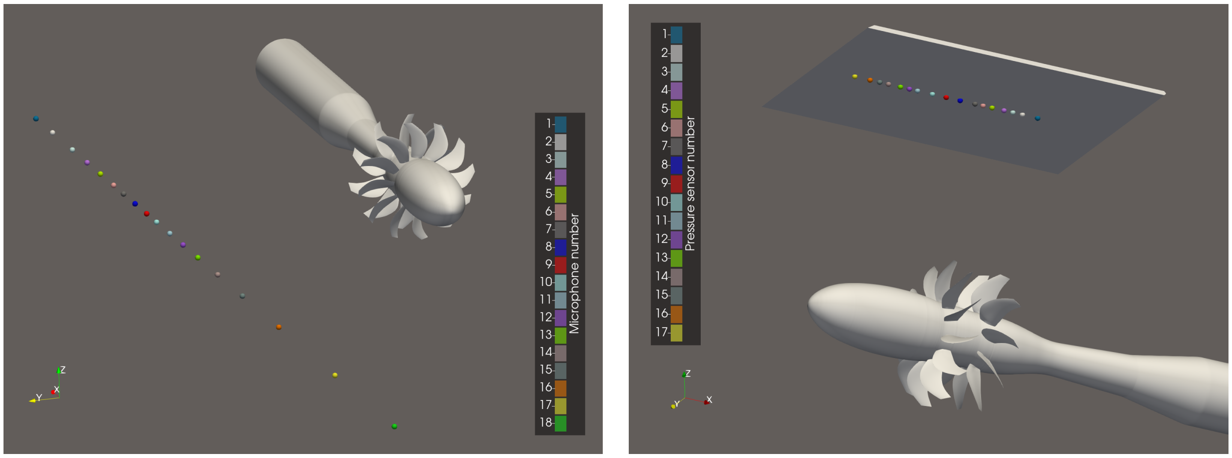

(a) Takeoff

(b) Cruise (with acoustic plate)

Fig. 1 Geometries for the takeoff and cruise conditions. The sideline microphone and acoustic plate pressure sensor arrays are also shown for the takeoff and cruise cases respectively.

turned on to improve the robustness while the numerical dissipation is highly localized in regions with discontinuities. To handle complex geometries at high Reynolds numbers, an algebraic wall model is used in conjunction with an immersed boundary method that is highly robust for under-resolved thin features, small cavities, sharp edges/corners, etc. Two capabilities are provided to simulate rotating geometries. The first one is the sliding mesh capability, in which independently meshed rotating and stationary subdomains are coupled through time-accurate non-conformal interfaces that slide relative to one another. Another capability is the rotating wall boundary conditions, where the wall velocity at rotating surfaces is set to match the local rotational speed. While the first capability can be used for any rotating geometry, the rotating wall boundary conditions are only suitable for smooth and axisymmetric surfaces.

An in-situ acoustic solver, based on the FWH formulation, is developed and coupled with the GPU-accelerated CFD solver such that acoustics at off-body microphones can be computed on-the-fly during the simulations using near-field CFD data sampled on acoustic surfaces for subsonic flows, without requiring a large off-body grid to resolve the acoustic wave propagation from near-field to the microphones. The in-situ permeable FWH solver with WMLES is validated for noise generated from jets [16], a small quadrotor [17], and turbofans [18]. ScaLES has also been validated on a wide variety of CFD applications [19–25].

A unique aspect of the GPU solver, compared to other CFD codes, is that most of the work is compute-bound, so that high performance is achieved even on graphics-oriented, bandwidth-restricted devices, such as NVIDIA RTX 4090 and L40S GPU cards, which are far less expensive than higher memory bandwidth hardware, and make WMLES practical for use in an industrial setting. The combination of Cartesian methods and an explicit time stepping scheme yields extremely low memory requirements. For example, ScaLES can simulate around 8-10 million cells per GB of GPU memory depending on the complexity of the configuration. Simulations containing between 400 and 500 million cells are routinely performed on desktop computers containing just two NVIDIA RTX 4090 GPUs with 24 GB of memory each.

B. Problem Setup

For the low-speed takeoff conditions, the freestream static pressure and temperature are set to 96765 Pa (14.0346 psi) and 305.18 K (549.324 °R) respectively, whereas for the high-speed cruise conditions, the corresponding freestream static pressure and temperature are 78230 Pa (11.3464 psi) and 296.05 K (532.885 °R). We simulate the two conditions using the physical (uncorrected) rotational speeds for the rotors, which are 6487 RPM and 6942 RPM for the takeoff and cruise conditions respectively.

For the low-speed takeoff conditions, three different Cartesian octree grids, labeled as grids A, A^+, and B^+ are constructed to examine the effects of grid topology and resolution on the aerodynamics and aeroacoustics. Cross-sections of these three grids are shown in Fig. 2. In both grids A and A^+, the finest cells, with grid spacing of 0.4 mm, are placed near the nacelle forebody, the front and aft blades, the front and aft rotating hubs, and the region between the

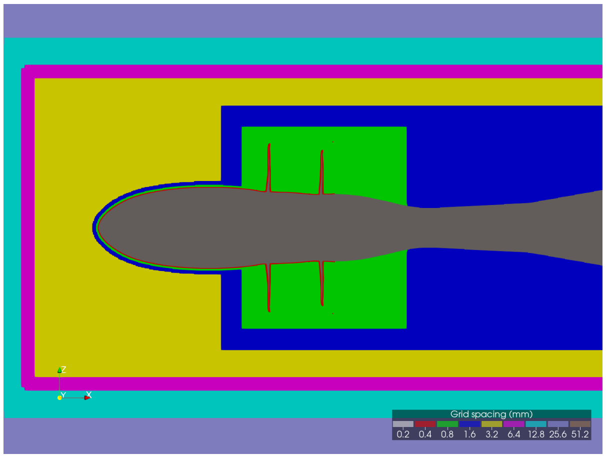

(a) Grid A (xz center-plane)

(b) Grid A (yz plane near the front blade tip)

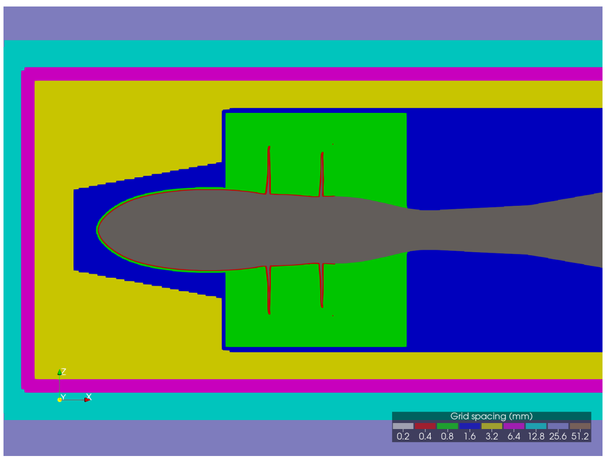

(c) Grid A^+ (xz center-plane)

(d) Grid A^+ (yz plane near the front blade tip)

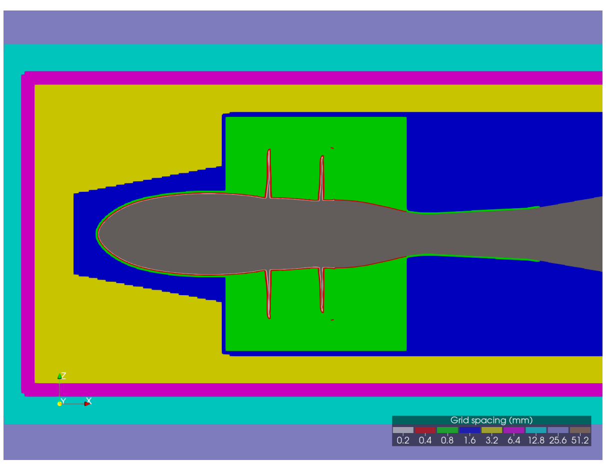

(e) Grid B^+ (xz center-plane)

(f) Grid B^+ (yz plane near the front blade tip)

Fig. 2 Cross-sections of different grids showing the grid topologies with the grid spacings for the takeoff conditions.

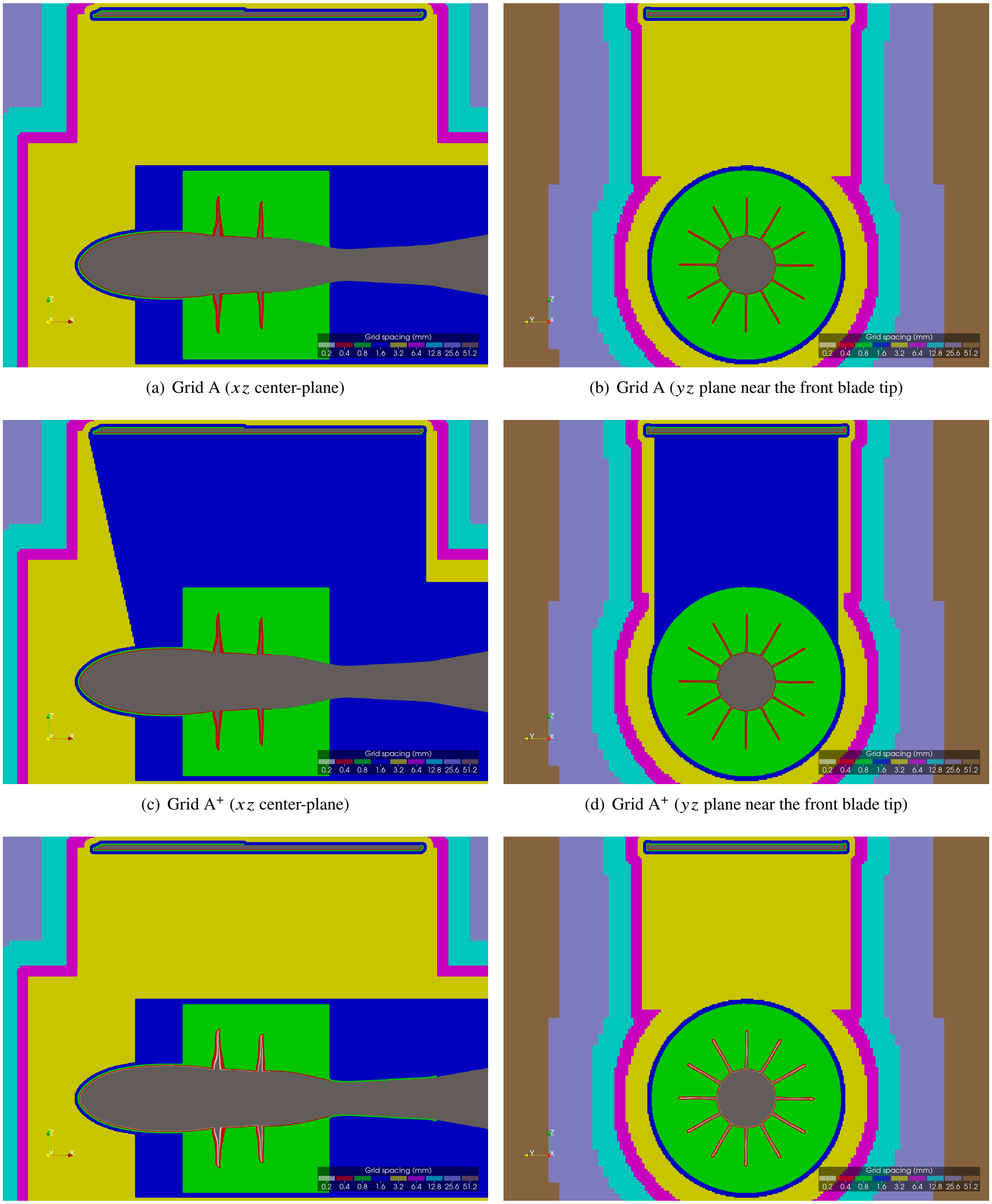

(a) Grid A (xz center-plane)

(b) Grid A (yz plane near the front blade tip)

(c) Grid A$^+$ (xz center-plane)

(d) Grid A$^+$ (yz plane near the front blade tip)

(e) Grid B (xz center-plane)

(f) Grid B (yz plane near the front blade tip)

Fig. 3 Cross-sections of different grids showing the grid topologies with the grid spacings for the cruise conditions.

trailing edge of the front rotating hub and the leading edge of the aft hub. In grid A, the rotating blades and hubs are enclosed by a cylindrical refinement region with grid spacing of 0.8 mm, which is itself surrounded by a second cylindrical refinement region with grid spacing of 1.6 mm extending farther downstream. Grid A^+ differs from grid A by the addition of a tapered cylindrical refinement region with grid spacing of 1.6 mm upstream of the nacelle forebody and the two cylindrical refinement regions. Finally, based on the grid A^+, the grid B^+ is generated by increasing the near-wall refinement of all solid surfaces by one additional grid level, resulting in a finest grid spacing of 0.2 mm near the forebody of the nacelle and all rotating surfaces.

Three grids are also constructed for the high-speed cruise conditions, which are labeled as grids A, A^+, and B. Cross-sections of the three grids are shown in Fig. 3. Grid A of the cruise case has a grid topology very similar to that of the grid A of the takeoff case near the CROR geometry, except that an additional large box-shaped refinement region with grid spacing of 3.2 mm is added between the CROR and the acoustic plate in order to resolve the direct propagation of acoustic waves from the rotors to the pressure sensors on the plate. In the vicinity of the plate surface facing the CROR, the grid is refined to the finest grid spacing of 0.4 mm to better resolve the boundary layer and the associated broadband pressure fluctuations. Grid A^+ is similar to the grid A, except that the direct propagation region is further refined by one more grid level. By contrast, grid B is built on grid A with one additional level of refinement near all rotating parts and the forebody of the nacelle.

To simulate the rotating geometries, the capabilities of sliding mesh and rotating wall boundary conditions are both employed. The sliding mesh capability is mainly used to enable the rotation of the blades with their corresponding hubs in the simulations. In order to do that, two axisymmetric rotating zones are defined to represent the rotating mesh regions, separated from the surrounding stationary mesh. These rotating zones are designed to be compact around the front and aft blade rows, such that the sliding mesh interfaces between the rotating and static meshes are placed as close to the rotating geometries as possible. The rotating mesh regions for both takeoff and cruise conditions are shown in Fig. 4. As mentioned above, a rotating seal is located between the front and aft rotor hubs and rotates together with the front hub. Its motion is modeled using rotating wall boundary conditions. The effects of the forward rotating seal on its boundary layer can also be visualized through the instantaneous contours of skin friction magnitude coefficient on the geometry surface, shown in Fig. 4.

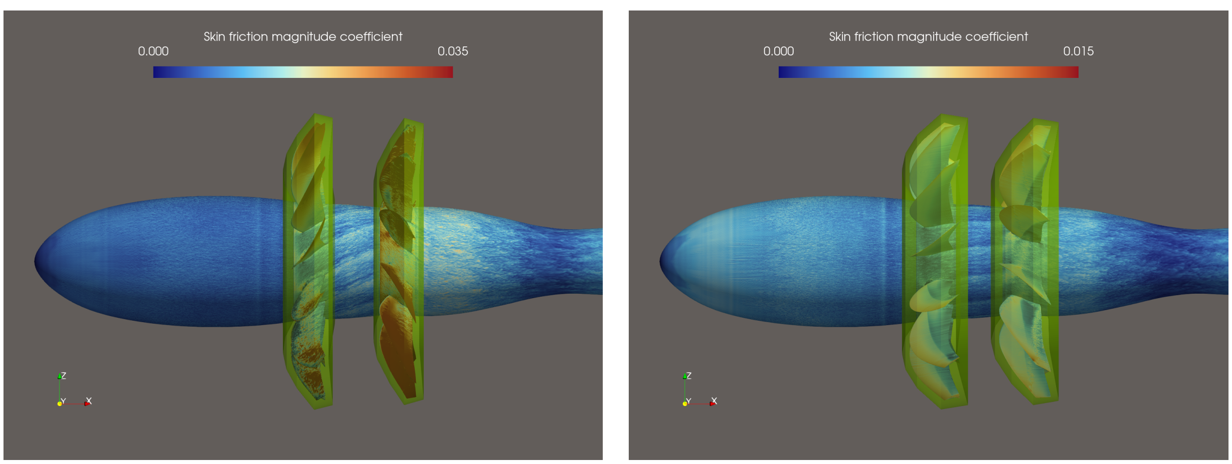

(a) Takeoff conditions on grid B^+

(b) Cruise conditions on grid B

Fig. 4 Sliding mesh regions, shown as transparent green volumes, for the takeoff and cruise conditions. The instantaneous skin friction magnitude coefficient is shown on the geometry surface.

All simulations are initialized with the freestream conditions and are run for 20 revolutions. Flow statistics are collected from the 5th revolution onward, after the initial transient is flushed out for each simulation. The details of all simulations including the grid statistics and the computational resources used are summarized in Tables 1 and 2. Fig. 5 shows the time histories of the thrust against the revolution for the simulations under the takeoff conditions. From the figure, it can be seen that the thrust has reached a statistically stationary state by the 5th revolution. The time-averaged thrust values for grids A, A^+, and B^+ are 2531.82, 2522.27, and 2536.15 N respectively, corresponding to differences of 1.23%, 1.60%, and 1.06%, relative to the experimental value of 2563.30 N [3]. These differences are comparable to or even smaller than those reported in earlier studies based on large eddy simulations or hybrid RANS/LES approaches [9, 11].

Table 1 Simulation details and computational resources for the takeoff conditions.

Grid	A	A^+	B^+
Minimum grid spacing [mm]	0.4	0.4	0.2
Number of compute grid cells [million]	894.4	1129	1480
Number of time steps per revolution	~26000	~26000	~58000
Number of revolutions	20	20	20
GPUs used	8x NVIDIA L40S	8x NVIDIA RTX PRO 6000	8x NVIDIA RTX PRO 6000
Wall-clock time per revolution [h]	1.41	0.80	2.06

The time-domain FWH formulation [26] in the permeable/porous form [27, 28] is used as the acoustic analogy to approximate noise at off-body observers with the near-field CFD data for the low-speed takeoff case. The time-domain FWH method is implemented in Volcano ScaLES as a streaming in-situ algorithm, such that acoustic waves can be propagated on-the-fly to microphones in the linear acoustic regions using the near-field data sampled on one or more FWH surfaces during the simulations, without the need to output the surface data to disk for later post-processing. This approach eliminates the need for large disk space for FWH surface data and also reduces the input/output (I/O) cost associated with reading and writing these data, which can otherwise become a bottleneck in both the simulations and the subsequent acoustic post-processing. Further details of the permeable FWH acoustic analogy are given in [16].

Two FWH surface designs, shown in Fig. 6, are used to examine the sensitivity of the acoustic predictions to the surface location. These are denoted as FWH surfaces A and B. Both surfaces fully enclose the entire CROR geometry and extend downstream with five staggered endcaps separated by 0.1 m. The far-field pressure fluctuations obtained from these endcaps are then averaged as a filtering procedure to reduce the spurious low-frequency contamination generated when the rotor wake passes through the downstream FWH caps [29, 30]. The main geometric difference between FWH surfaces A and B is in the upstream region around the nacelle forebody. FWH surface A has a simple cylindrical shape with a constant radius of 0.42 m over its full length. In contrast, FWH surface B retains a cylindrical main body over most of its length but replaces the upstream cylindrical section with a tapered nose-like section that follows the nacelle forebody more closely. As seen in Fig. 6, this tapered upstream section makes FWH surface B more compact near the inlet and reduces the offset between the FWH surface and the solid geometry in the upstream direction. An annular face, that faces upstream, connects the tapered nose section to the constant-radius cylindrical main section. The key idea in the FWH design is to position the FWH surface closer to the dominant noise sources (the rotors and the wake) while ensuring it remains outside regions of significant quadrupole activity. The effects of using a tighter FWH surface (surface B against surface A) around the nacelle forebody and the front rotor will be studied.

The cross-sections of the FWH surfaces used in the different simulations are shown in Fig. 7, together with the

Table 2 Simulation details and computational resources for the cruise conditions.

Grid	A	A^+	B
Minimum grid spacing [mm]	0.4	0.4	0.2
Number of compute grid cells [million]	1285	1492	1632
Number of time steps per revolution	~27000	~27000	~58000
Number of revolutions	20	20	20
GPUs used	8x NVIDIA L40S	8x NVIDIA L40S	8x NVIDIA RTX PRO 6000
Wall-clock time per revolution [h]	1.52	1.70	2.86

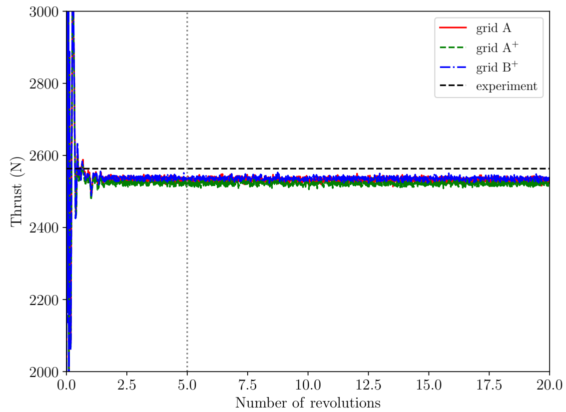

Fig. 5 Time histories of the thrust. The vertical gray dotted line indicates the time when time-averaging starts.

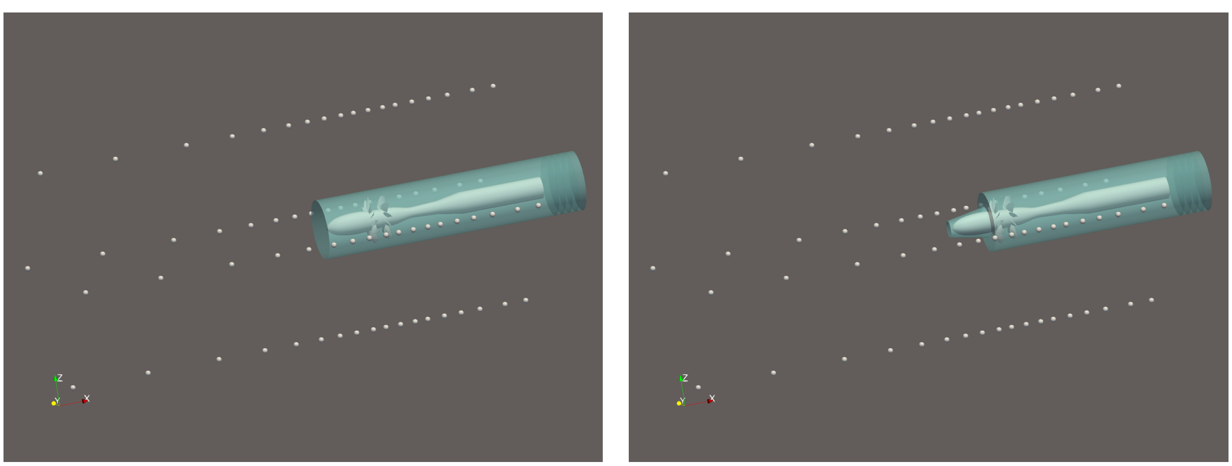

(a) FWH surface A

(b) FWH surface B

Fig. 6 FWH surfaces for the takeoff conditions. Four azimuthally repeated microphone arrays are used for ensemble-averaging.

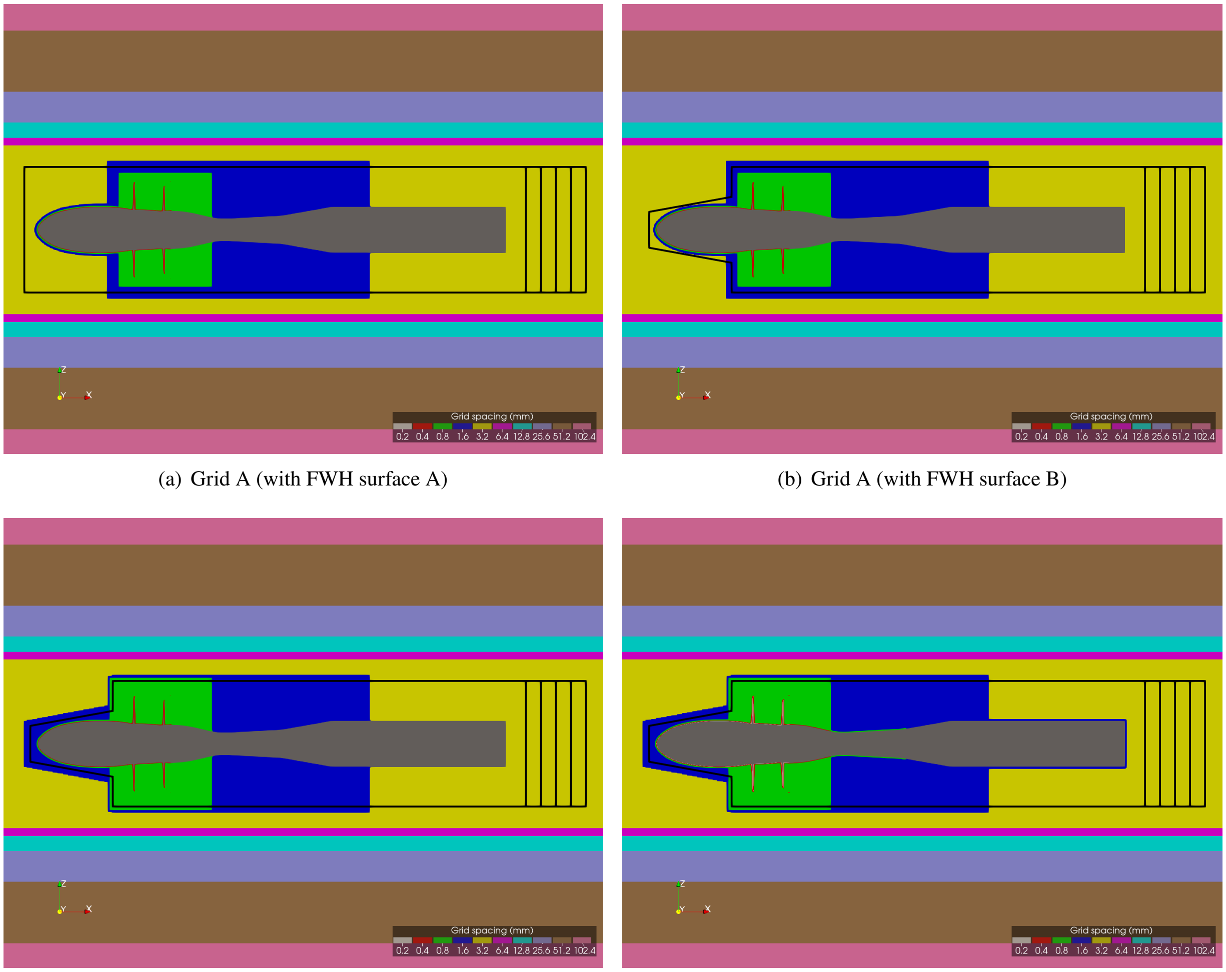

(a) Grid A (with FWH surface A)

(b) Grid A (with FWH surface B)

(c) Grid A$^+$ (with FWH surface B)

(d) Grid B$^+$ (with FWH surface B)

Fig. 7 Cross-sections of FWH surfaces used for different grids in the xz center-plane, where the grid topologies are also shown, for the takeoff conditions.

corresponding grid topologies in the xz center-plane. For grid A, both FWH surfaces A and B are considered. In the case with FWH surface A, the entire upstream portion of the surface lies within the coarser 3.2 mm grid region. In contrast, for FWH surface B, the tapered upstream section penetrates into the finer near-body refinement region, so that the upstream-facing surface connecting the tapered nose and the constant-radius cylindrical sections is located in the 1.6 mm grid zone. The FWH surfaces are triangulated with an approximate edge length of 4 mm. Grid A$^+$ further extends this upstream grid refinement such that the entire upstream portion of FWH surface B lies within the 1.6 mm region. For grid B$^+$, the near-wall grid is further refined, while the grid resolution in the region occupied by FWH surface B remains essentially the same as that in grid A$^+$. The grid A simulation is performed with both FWH surfaces A and B, whereas the grid-A$^+$ and grid-B$^+$ simulations are performed only with FWH surface B. Although only one microphone array is available in the experiment, four repeated microphone arrays are used in the simulations, as shown in Fig. 6, so that the acoustic signals can be statistically improved through ensemble averaging by exploiting the axisymmetry of the configuration.

IV. Computational Results and Discussion

Fig. 8 compares the instantaneous velocity dilatation fields, normalized by the period of one rotor revolution, for the takeoff and cruise conditions. For the low-speed takeoff case on grid B$^+$, it is shown that the dilatation has large magnitude in the shear layers associated with the rotor tip vortices. Away from the wake and the CROR, the dilatation field becomes weak, although weak outward-propagating acoustic waves are still visible. By contrast, the high-speed cruise case on grid B shows much stronger and more coherent dilatation structures generated by shock waves originating from the blades. These shocks propagate from the CROR toward the acoustic plate and are reflected there, while strong dilatation is also present within the boundary layer over the plate. The figure therefore indicates that acoustic propagation is predominantly linear in the takeoff case, whereas nonlinear effects are large in the cruise case because of the presence of shocks between the CROR and the acoustic plate. Accordingly, different acoustic prediction strategies are adopted for the two operating conditions. For the takeoff case, near-field CFD data are sampled on a permeable FWH surface surrounding the CROR, and the acoustic propagation from the near-field to the observer microphones is approximated using the in-situ FWH solver. For the cruise case, however, the use of a permeable FWH surface is problematic because shock discontinuities outside the surface may have a substantial contribution to the omitted quadrupole term in the acoustic formulation. In addition, the passage of shocks through the FWH surface may result in serious contamination of the acoustic calculations as the integrand of the FWH equation becomes non-smooth. Since the shock system lies between the CROR and the acoustic plate, it is difficult to define a surface that both surrounds the relevant source region and avoids shock interference. A direct noise computation approach is therefore used instead, in which the nonlinear acoustic wave propagation from the rotors to the sensors on the acoustic plate is simulated directly using sufficiently fine CFD grid resolution.

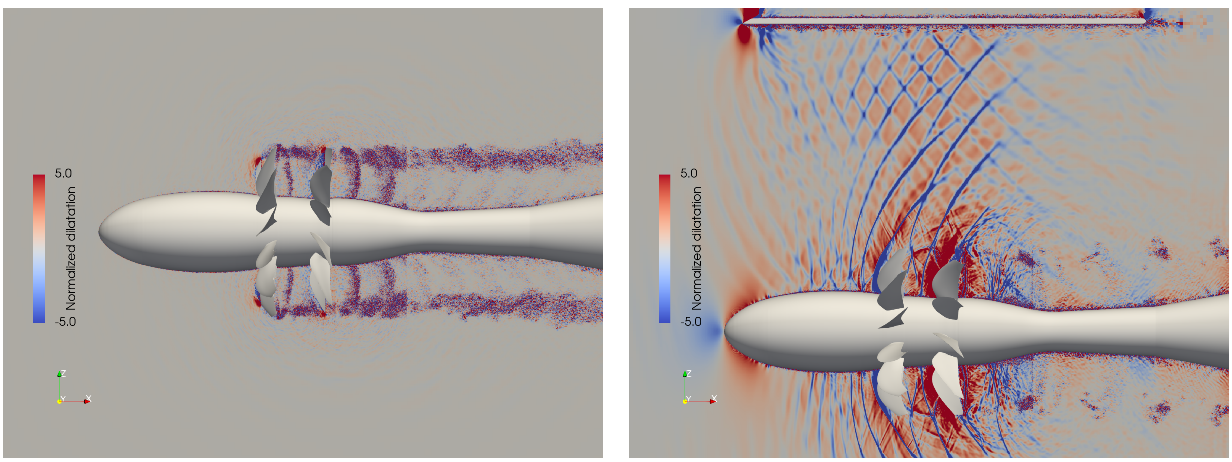

(a) Takeoff conditions on grid B$^+$

(b) Cruise conditions on grid B

Fig. 8 Comparison of instantaneous velocity dilatation, normalized by the time period of one rotor revolution, in the xz center-plane for the takeoff and cruise conditions.

3D particle image velocimetry (PIV) flow field measurements were acquired in a volume between the front and aft blade rotors in NASA's 9- by 15-ft LSWT [31]. Measurements were obtained for several low-Mach operating conditions using phase-averaging with the phase referenced with the front rotor such that there are 12 phase step measurements per revolution. Two phase steps of the forward rotor were acquired for each operating condition in the experiment. In the present comparison, we have chosen the case corresponding to the 0° phase step and a front rotor rotational speed of 6444 RPM. Fig. 9 compares the phase-averaged velocity magnitude, computed from the phase-average velocity components, between the simulations and the PIV measurements at several cut-planes. From the comparison, we can observe that the wake of the blades, the shear layer, and the tip vortices are reasonably well captured in the simulations. Fig. 10 shows a more detailed comparison of the phase-averaged velocity magnitude in the xz center-plane. The PIV measurements show two tip vortex signatures in this plane. The upstream tip vortex is captured in the simulations on all three grids. However, the magnitude of the downstream tip vortex on grids A and A$^+$ is weaker than that in the experiment. With the additional near surface refinement in grid B$^+$, particularly near the blade surface, we can see that the downstream vortex is better resolved, suggesting that the additional near surface grid refinement improves the resolution of the front rotor wake and its interaction with the aft rotor.

Fig. 11 compares the power spectral density (PSD) spectra of the pressure fluctuations at selected microphones between the simulations and the experimental measurements (D074-470 [3]) for the low-speed takeoff conditions. The

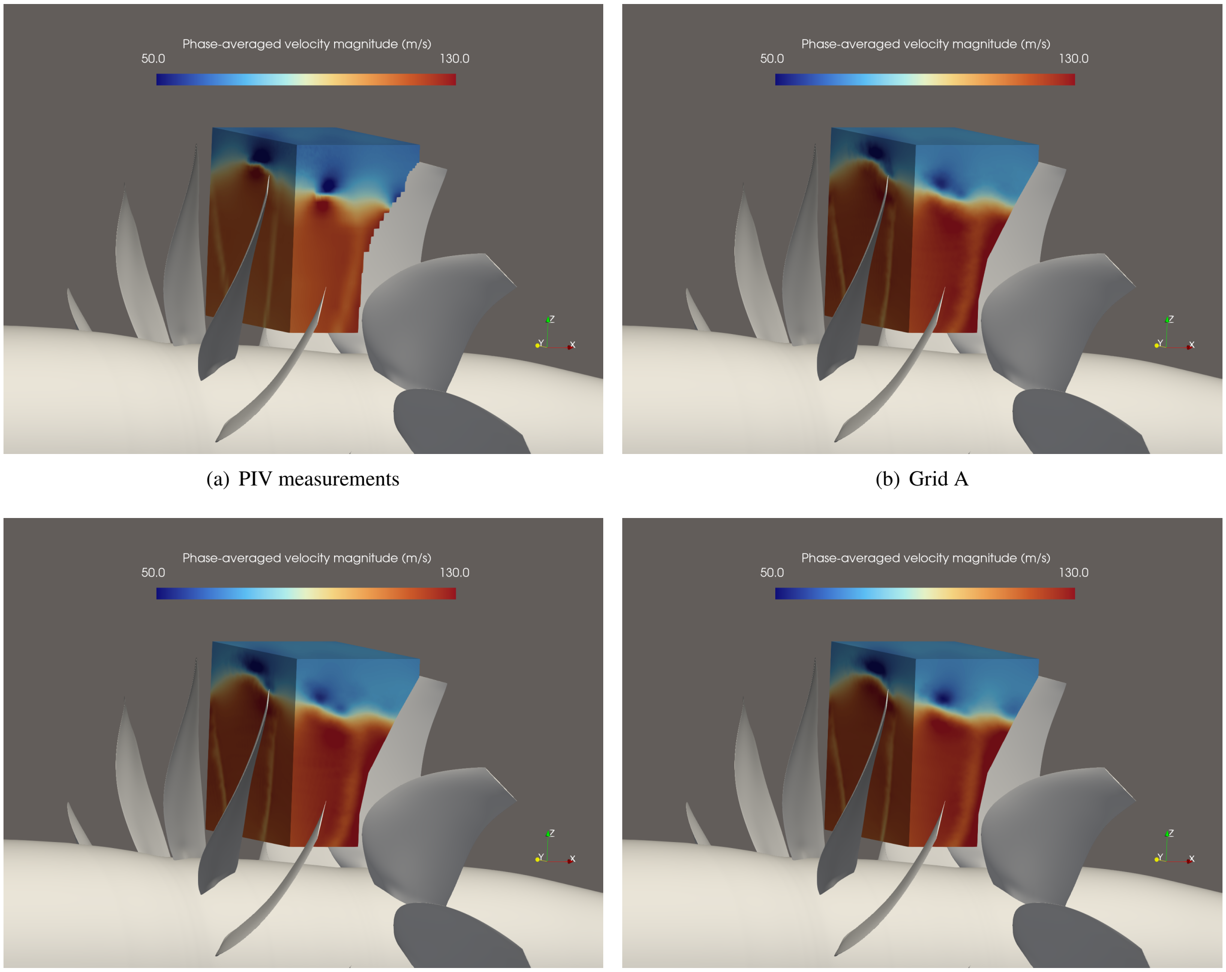

(a) PIV measurements

(b) Grid A

(c) Grid A$^+$

(d) Grid B$^+$

Fig. 9 Comparison of phase-averaged velocity magnitude at different cut-planes for the takeoff conditions.

simulated PSD spectra are computed from pressure fluctuation signals at the microphones, obtained using the in-situ FWH solver and sampled at 100 kHz, using the Welch's method. The time series is divided into 10 segments with 75% overlap and the Hann window is applied to each window. Each segment contains 4000 samples, corresponding to a frequency resolution of 25 Hz. In addition, ensemble averaging over the four repeated microphone arrays is applied to improve statistical convergence, with the four arrays treated as equivalent realizations by exploiting the rotational symmetry of the configuration. In Fig. 11, frequency is expressed in shaft order by normalizing with the rotor rotation frequency. The horizontal axis spans shaft orders 8 to 150, corresponding to 864.93-16217.5 Hz. As shown in Fig. 11, the simulations generally capture the overall broadband levels and the main tonal features with reasonable fidelity at microphones #3, #8, #13, and #18, ordered here from downstream to upstream locations, although noticeable differences remain in the amplitudes of individual tones. For microphones #3, #8, and #13, the spectra obtained with different grids and FWH surfaces are similar, which indicates limited sensitivity to the numerical setup within the shaft order range examined here. Microphone #18 exhibits the largest discrepancy among the four chosen locations. In particular, results from grid A with FWH surface A show a pronounced under-prediction of the noise level at higher shaft order range, while the other three cases using FWH surface B follow the experimentally measured spectra much better. This suggests that the FWH surface shape and placement have a stronger effect on the predicted signal at upstream observer locations, such as microphone #18. The zoomed comparison in Fig. 12 further shows that, at microphone #8, the amplitudes of fundamental tones at shaft orders 10 and 12, corresponding to the aft and front rotor blade-passing frequencies, respectively, are in reasonable agreement with the measurements. Several harmonics, including those at shaft orders 20,

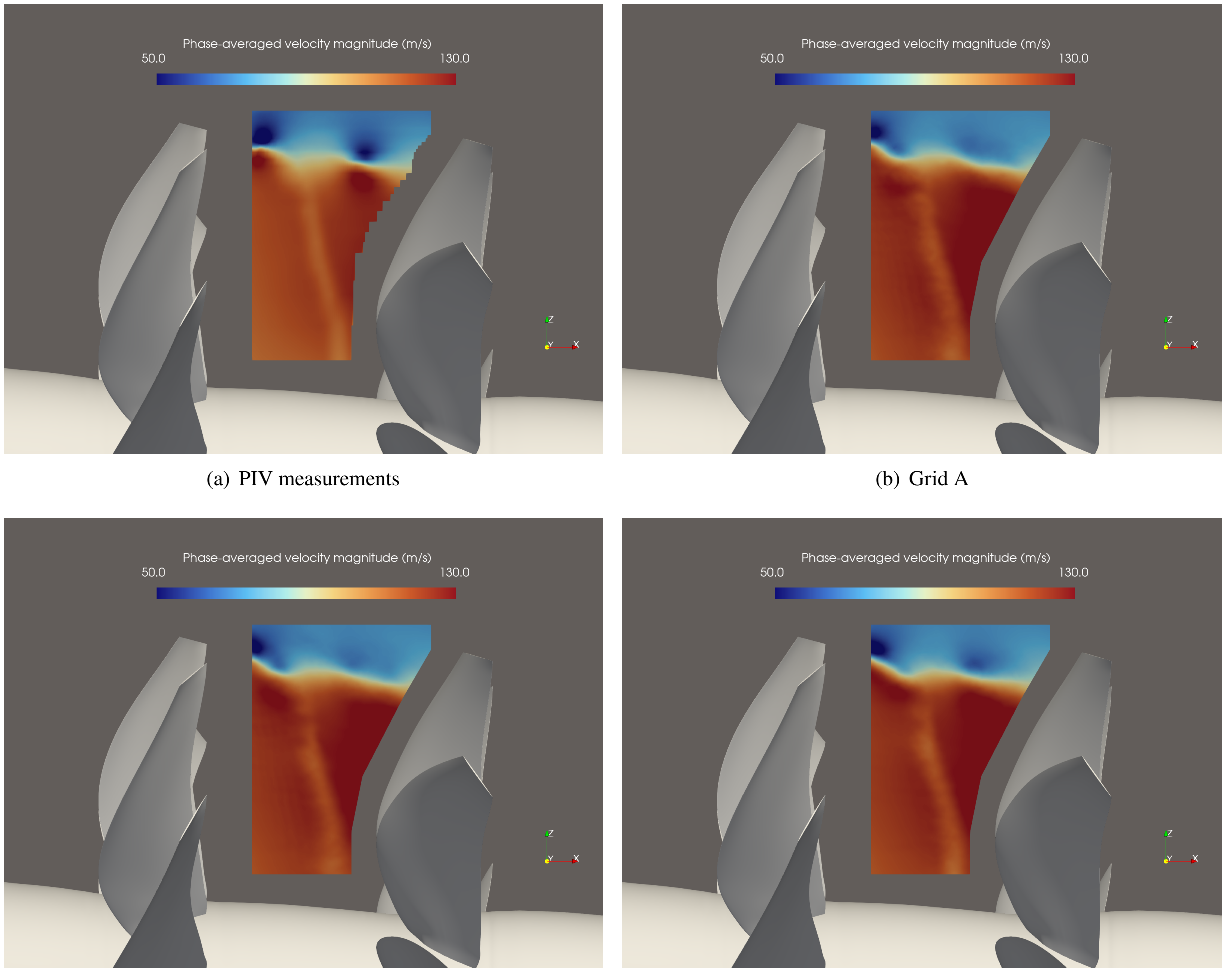

(a) PIV measurements (b) Grid A

(c) Grid A^{+} (d) Grid B^{+}

Fig. 10 Comparison of phase-averaged velocity magnitude in the xz center-plane for the takeoff conditions.

24, 30, 36, and 40, are also reproduced at the correct shaft orders, although differences in peak amplitude remain and the experimental peaks are often stronger and sharper. This difference may be caused by the finer frequency resolution used in the experiment, which is approximately 12 Hz (with more samples per segment of signal). The zoomed spectra further show that, in addition to the primary blade-passing tones at shaft orders 10 and 12 and their harmonics, several interaction tones at shaft orders 22, 32, 34, 42, 44, and 46 are also captured. These peaks are consistent with linear combinations of the front and aft rotor blade-passing frequencies and indicate that the simulations reproduce not only the single-rotor tonal content but also part of the rotor-rotor interaction signature. There are also some large tonal peaks at odd shaft orders, such as at shaft order 13, in the experimental spectra. These are not expected to occur in theory for an ideal CROR setup and are not predicted in the simulations. As discussed in [6], the blades in the actual rotor disks are not manufactured identically but instead exhibit small random variations in pitch angle, within approximately $\pm 0.25°$. As a result, there is some leakage of energy from the theoretically expected tones to the odd tones in the experiments. By comparison, once FWH surface B is used, the differences among grids A, A^{+}, and B^{+} are relatively small, suggesting that grid A already provides an adequate resolution for the acoustic predictions and that the results are only weakly affected by further grid refinement.

Fig. 13 compares the narrow-band sound pressure level (SPL) spectra at the pressure sensors #1, #5, #9, and #13, ordered here from downstream to upstream locations, on the acoustic plate between the simulation and experimental measurements (D106-2962 [3]) for the high-speed cruise conditions. The SPL spectra are obtained by first computing the PSD spectra of the pressure fluctuation signals sampled at 100 kHz using the Welch's method, and then converting the

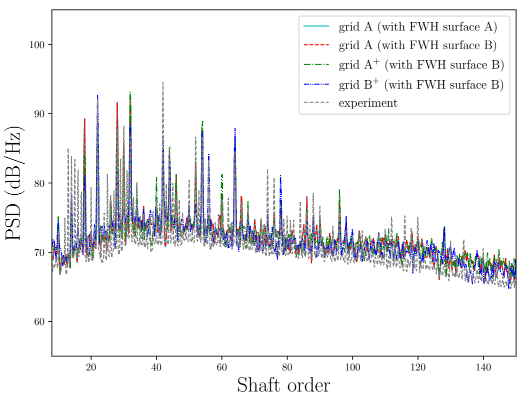

(a) Microphone #3

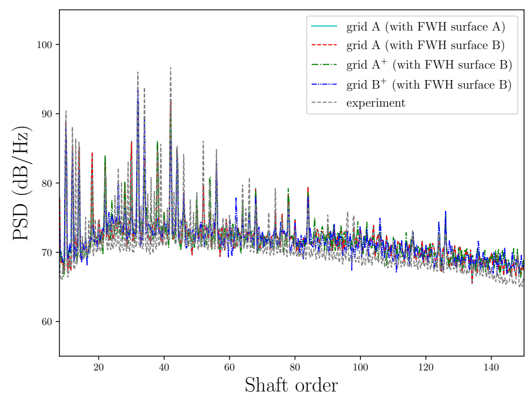

(b) Microphone #8

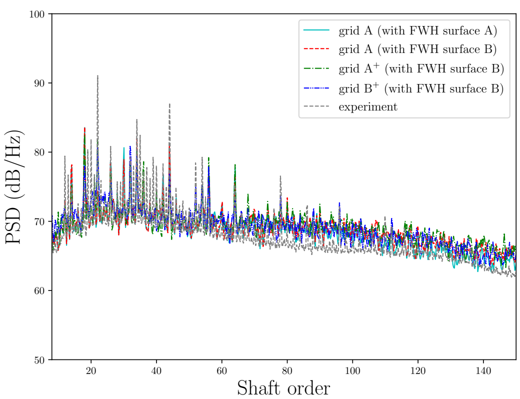

(c) Microphone #13

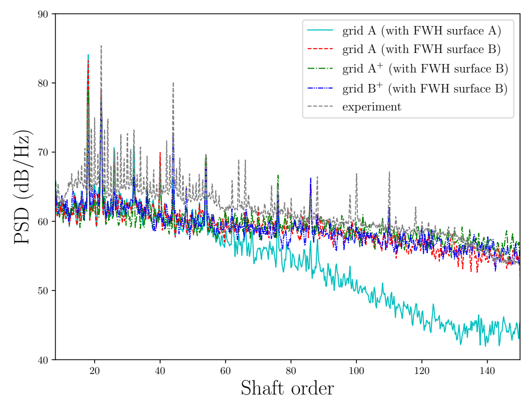

(d) Microphone #18

Fig. 11 Comparison of PSD spectra at selected microphones for the takeoff conditions.

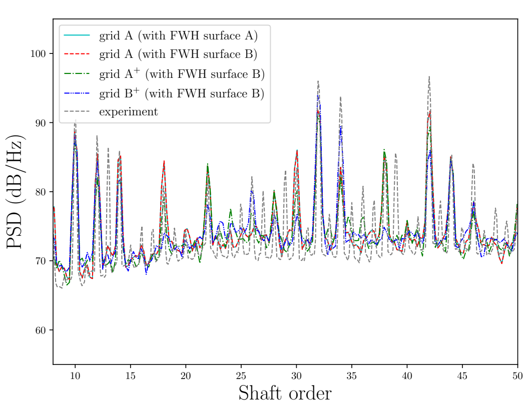

(a) Microphone #8

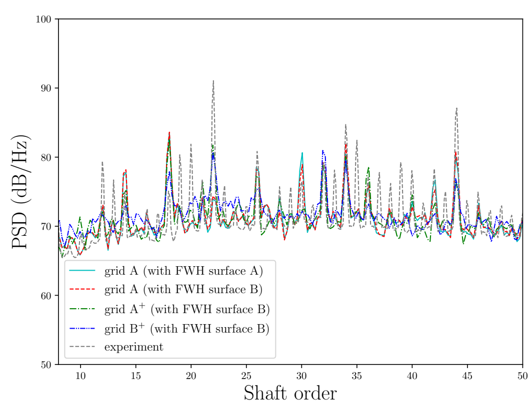

(b) Microphone #13

Fig. 12 Comparison of PSD spectra in a narrower shaft order range at selected microphones for the takeoff conditions.

PSD to SPL. The time series are truncated into 9 windows (bins) with 75% overlap and Hann windowing. Each window contains 4000 samples, corresponding to a frequency resolution of 25 Hz. The frequency in Fig. 13 is normalized into shaft order using the frequency for one rotor revolution. The horizontal axis spans shaft orders 8 to 150, corresponding to 925.6 - 17355 Hz. In general, the simulations reproduce the overall spectral trends and the locations of several dominant tonal peaks, but they generally under-predict the measured broadband levels by roughly 5-10 dB in the low shaft order range. Similar levels of under-prediction in broadband noise were also shown in previous works [6, 11]. This discrepancy may reflect additional physical contributions to the pressure signals measured at the sensors on the acoustic plate, including wind tunnel background noise and the reflection of acoustic waves from the wind tunnel walls. The broadband noise levels predicted by simulation results on the three grids are similar, which suggests limited sensitivity to the grid refinements, such as refinement of the volume grid for direct noise propagation, or near surface grid refinement, considered here. The zoomed spectra in Fig. 14 further show that many of the dominant tonal peaks are captured at the correct shaft orders, and that their amplitudes are predicted reasonably well at shaft orders 10, 12, 20, 24, 30, 36, and 40, which correspond to harmonics of the blade-passing frequencies of the front and aft rotors. The zoomed spectra also show that, besides the dominant tonal peaks at shaft orders 10 and 12, several pronounced peaks also appear at shaft orders 22, 32, 34, 42, 44, and 46, as in the takeoff case. These peaks are consistent with rotor-rotor interaction tones, which are combination tones formed from the blade-passing frequencies of the aft and front rotors and their harmonics. The simulations capture many of these interaction tones reasonably well, although the corresponding amplitudes are often under-predicted. The experimental spectra also contain weaker tones at odd shaft orders. As discussed for the takeoff case, this is caused by the manufacturing imperfection of the blades, which leads to the leakage of energy from the theoretically expected tones into neighboring odd shaft orders. At some shaft orders, grid A^+ clearly predicts stronger tonal peaks than grids A and B, such as at shaft order 32 at sensor #5 and shaft order 40 at sensor #9, but the overall differences among the simulations are small for the captured tonal peaks.

V. Concluding Remarks

A GPU-accelerated wall-modeled large eddy simulation solver, Volcano ScaLES, has been applied to the F31/A31 counter-rotating open rotor configuration under representative low-speed takeoff and high-speed cruise conditions. For the takeoff conditions, the simulations with different grid topologies and resolution reproduced the main measured flow features, predicted thrust accurately, and captured the overall broadband and tonal acoustic characteristics with high fidelity. The takeoff case study further showed that, once a well-designed FWH surface is placed sufficiently close to the near-body acoustic sources while remaining outside regions of significant quadrupole activity, the smallest and coarsest grid can already provide good acoustic predictions, and that the results are only weakly sensitive to additional grid refinements within the shaft order range considered here.

For the cruise conditions, shock structures were observed between the rotor system and the acoustic plate, indicating that nonlinear propagation effects are important and motivating the use of direct noise propagation rather than the hybrid CFD and FWH approach. The computationally predicted narrowband SPL spectra with different grids reproduced the overall spectral trends and many of the dominant tonal peaks, including rotor-rotor interaction tones, although the measured broadband levels were under-predicted in the lower shaft order range, similar to previous numerical studies. The comparison among grids with different grid topologies and resolution also showed relatively small differences in the predicted spectra, demonstrating that the coarsest and smallest grid already provides good predictions on acoustics considered here, and the further grid refinements in the direct noise propagation regions or near-body regions have small effects on the acoustic results.

An important practical outcome of the present study is that the coarser grids already appear to provide adequate resolution to predict aeroacoustics for both the takeoff and cruise cases considered here. At this grid level, a simulation with 20 revolutions requires approximately one day per case. These computations were carried out using only single node servers equipped with 8 workstation GPUs, without reliance on a large high performance computing cluster. The results therefore demonstrate that the present framework can provide useful CROR aeroacoustic predictions with practical turnaround time on relatively modest computational hardware, highlighting its potential as a practical design and analysis tool for aeroacoustics of open rotors.

Acknowledgments

This work has been supported by NASA Small Business Innovation Research (SBIR) Phase-I and Phase-II programs with contract numbers: 80NSSC24PB479 and 80NSSC25C0002 respectively. We gratefully acknowledge Dr. David

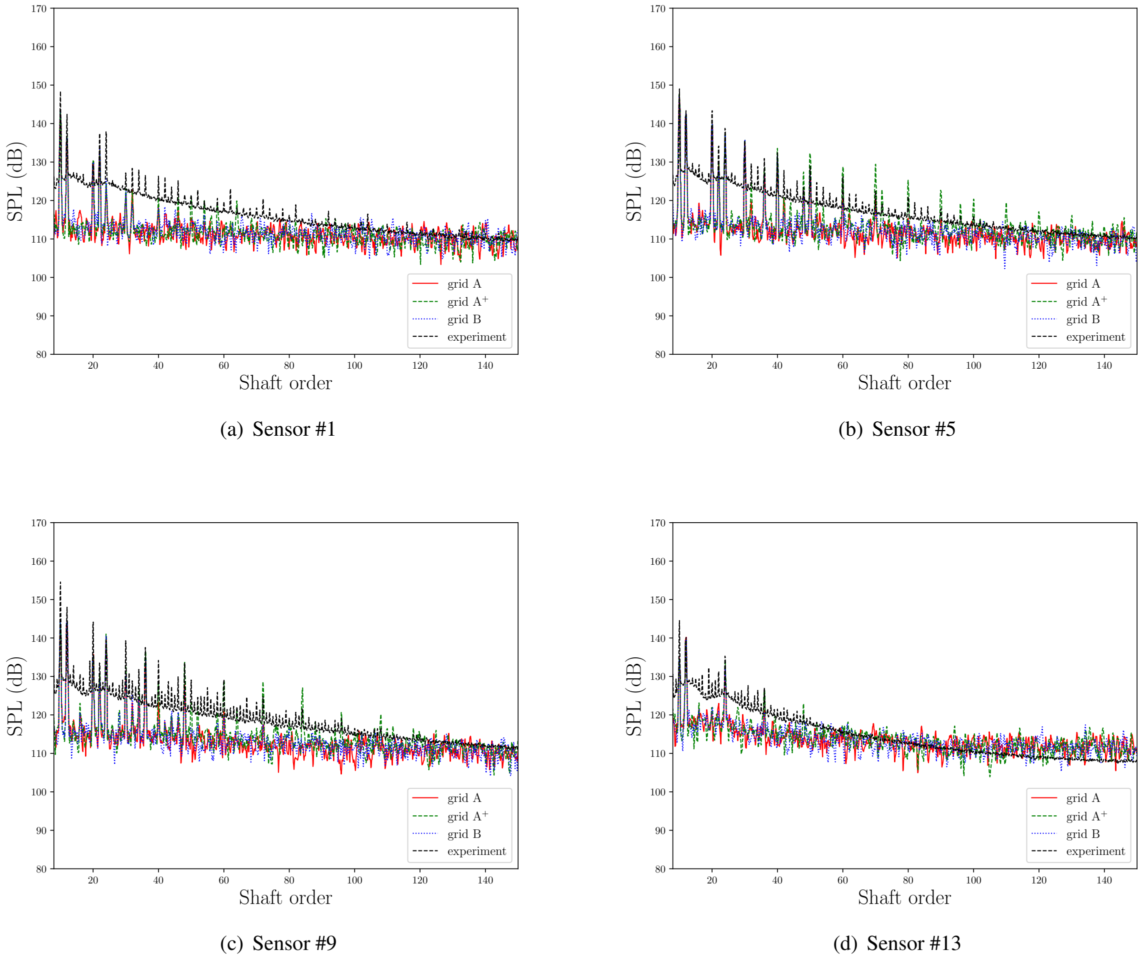

(a) Sensor #1 (b) Sensor #5

(c) Sensor #9 (d) Sensor #13

Fig. 13 Comparison of SPL spectra at selected pressure sensors for the cruise conditions.

Stephens of the NASA Glenn Research Center for serving as the technical monitor, sharing the experimental data, and providing insightful contributions. We also greatly appreciate Dr. Edmane Envia of NASA Glenn Research Center for his valuable discussions.

References

[1] Van Zante, D., Gazzaniga, J., Elliott, D., and Woodward, R., "An open rotor test case: F31/A31 historical baseline blade set," *ISABE 2011-1310*, 2011.

[2] Stephens, D., "Nearfield unsteady pressures at cruise Mach numbers for a model scale Counter-Rotation Open Rotor," *18th AIAA/CEAS Aeroacoustics Conference (33rd AIAA Aeroacoustics Conference)*, 2012, p. 2264.

[3] Stephens, D. B., "Data Summary Report for the Open Rotor Propulsion Rig Equipped With F31/A31 Rotor Blades," Tech. Rep. NASA/TM–2014-216676, 2014.

[4] Stephens, D., and Sree, D., "Tone and broadband noise separation from acoustic data of a scale-model counter-rotating open rotor," *20th AIAA/CEAS Aeroacoustics Conference*, 2014, p. 2744.

[5] Khalid, S. A., "Progress in open rotor propulsors: The FAA/GE/NASA open rotor test campaign," *The Aeronautical Journal*, Vol. 118, No. 1208, 2014, pp. 1181–1213.

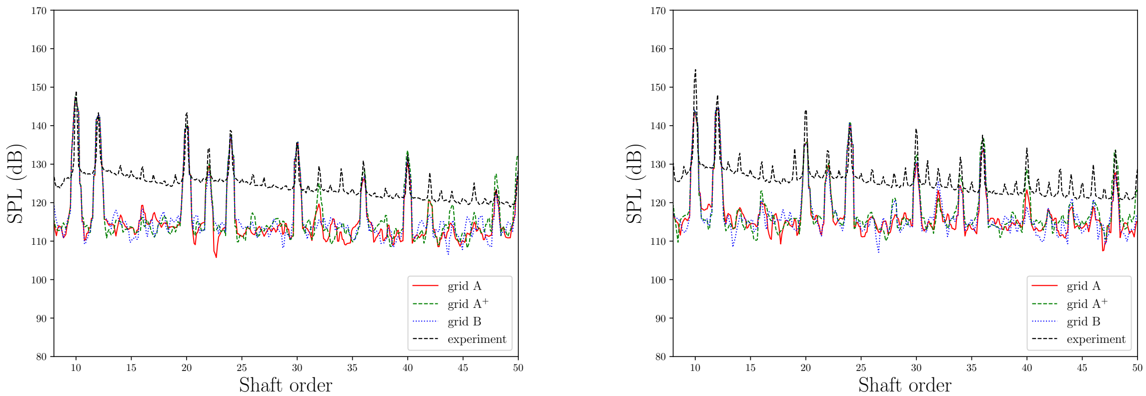

(a) Sensor #5 (b) Sensor #9

Fig. 14 Comparison of SPL spectra in a narrower shaft order range at selected pressure sensors for the cruise conditions.

[6] Envia, E., "Aeroacoustic analysis of a high-speed open rotor," *International Journal of Aeroacoustics*, Vol. 14, No. 3-4, 2015, pp. 569–606.

[7] Soulat, L., Kernemp, I., Sanjose, M., Moreau, S., and Fernando, R., "Numerical assessment of the tonal noise of Counter-Rotating Open Rotors at approach," *International Journal of Aeroacoustics*, Vol. 15, No. 1-2, 2016, pp. 23–40.

[8] Nark, D. M., Jones, W., Boyd, D., and Zawodny, N., "Isolated open rotor noise prediction assessment using the F31A31 historical blade set," *54th AIAA Aerospace Sciences Meeting*, 2016, p. 1271.

[9] Brehm, C., Barad, M. F., and Kiris, C. C., "Development of immersed boundary computational aeroacoustic prediction capabilities for open-rotor noise," *Journal of Computational Physics*, Vol. 388, 2019, pp. 690–716.

[10] Dumlupinar, E., Housman, J. A., Kenway, G. K., and Kiris, C. C., "Unsteady RANS and Scale Resolving Simulations of Open Rotor Noise," *AIAA SciTech 2023 Forum*, 2023, p. 0028.

[11] Dumlupinar, E., Housman, J. A., and Duensing, J., "Scale Resolving Simulations of Contra Rotating Open Rotor Noise Prediction," *AIAA SCITECH 2024 Forum*, 2024, p. 2807.

[12] Moin, P., Squires, K., Cabot, W., and Lee, S., "A dynamic subgrid-scale model for compressible turbulence and scalar transport," *Physics of Fluids A: Fluid Dynamics*, Vol. 3, No. 11, 1991, pp. 2746–2757.

[13] Lilly, D., "A proposed modification of the Germano subgrid-scale closure method," *Physics of Fluids A*, Vol. 4, No. 3, 1992, pp. 633–635.

[14] Shu, C.-W., and Osher, S., "Efficient implementation of essentially non-oscillatory shock-capturing schemes," *Journal of computational physics*, Vol. 77, No. 2, 1988, pp. 439–471.

[15] Gottlieb, S., Shu, C.-W., and Tadmor, E., "Strong stability-preserving high-order time discretization methods," *SIAM review*, Vol. 43, No. 1, 2001, pp. 89–112.

[16] Wong, M. L., Ghate, A., Kenway, G. K., Angel, J. B., and Kiris, C. C., "Immersed Boundary Wall-Modelled Large Eddy Simulations of Subsonic Jet Flows and Acoustics," *AIAA AVIATION FORUM AND ASCEND 2024*, 2024, p. 4466.

[17] Wong, M. L., Kenway, G. K. W., Ghate, A. S., Angel, J. B., and Kiris, C. C., "Quadcopter Noise Predictions with Wall-Modeled Large Eddy Simulations," 2025.

[18] Ghate, A. S., Wong, M. L., Kenway, G., Angel, J. B., Kiris, E., , and Kiris, C. C., "Noise Prediction of Ducted Fans using Immersed Boundary Wall-Modeled Large Eddy Simulations," *32nd AIAA/CEAS Aeroacoustics Conference (2026)*, 2026.

[19] Kenway, G. K., Ghate, A., Browne, O. M., Wong, M. L., Angel, J. B., and Kiris, C. C., "Immersed Boundary Wall-Modelled Large Eddy Simulations of a Generic Hammerhead Payload Fairing," *AIAA AVIATION FORUM AND ASCEND 2024*, 2024, p. 3693.

[20] Ghate, A. S., Angel, J. B., Kenway, G., Wong, M. L., and Kiris, C. C., "Large Eddy Simulations of High-Lift Common Research Model in the NTF Wind Tunnel at Flight Scale Reynolds Numbers," *AIAA SCITECH 2026 Forum*, 2026, p. 0020.

[21] Ashton, N., Ghate, A., Kenway, G., Angel, J., Wong, M. L., and Kiris, C. C., "Immersed Boundary Wall-Modelled Large Eddy Simulations for the 5th High-Lift Prediction Workshop," *AIAA SCITECH 2025 Forum*, 2025, p. 0888.

[22] Wong, M. L., Ghate, A., Kenway, G. K., Angel, J. B., and Kiris, C. C., "Immersed Boundary Wall-Modelled Large Eddy Simulations of Straight Wings with Three-Dimensional Ice Accretion," *AIAA AVIATION FORUM AND ASCEND 2024*, 2024, p. 4000.

[23] Angel, J. B., Wong, M. L., Kenway, G., Ghate, A., and Kiris, C. C., "Validation of Immersed Boundary Wall-Modelled Large Eddy Simulations with F-16XL Flight Data," *AIAA AVIATION FORUM AND ASCEND 2024*, 2024, p. 4374.

[24] Angel, J. B., Ghate, A., Kenway, G., Wong, M. L., Kiris, C. C., and Ashton, N., "Immersed boundary wall-modelled large eddy simulations for automotive aerodynamics," *AIAA Aviation Forum and Ascend 2024*, 2024, p. 4172.

[25] Angel, J. B., Ghate, A., Kenway, G., Wong, M. L., and Kiris, C. C., "DLR LK6E2 Missile Airframe Validation Study Using Wall-Modeled Large Eddy Simulations," *AIAA SCITECH 2025 Forum*, 2025, p. 1949.

[26] Ffowcs Williams, J. E., and Hawkings, D. L., "Sound generation by turbulence and surfaces in arbitrary motion," *Philosophical Transactions for the Royal Society of London. Series A, Mathematical and Physical Sciences*, 1969, pp. 321–342.

[27] Di Francescantonio, P., "A new boundary integral formulation for the prediction of sound radiation," *Journal of Sound and Vibration*, Vol. 202, No. 4, 1997, pp. 491–509.

[28] Brentner, K. S., and Farassat, F., "Analytical comparison of the acoustic analogy and Kirchhoff formulation for moving surfaces," *AIAA journal*, Vol. 36, No. 8, 1998, pp. 1379–1386.

[29] Shur, M. L., Spalart, P. R., and Strelets, M. K., "Noise prediction for increasingly complex jets. Part I: Methods and tests," *International journal of aeroacoustics*, Vol. 4, No. 3, 2005, pp. 213–245.

[30] Mendez, S., Shoeybi, M., Lele, S., and Moin, P., "On the use of the Ffowcs Williams-Hawkings equation to predict far-field jet noise from large-eddy simulations," *International Journal of Aeroacoustics*, Vol. 12, No. 1-2, 2013, pp. 1–20.

[31] Van Zante, D., and Wernet, M., "Tip vortex and wake characteristics of a counterrotating open rotor," *48th AIAA/ASME/SAE/ASEE Joint Propulsion Conference & Exhibit*, 2012, p. 4039.